

**Original and pyrometamorphical altered Bentheimer sandstone  
Petrophysical properties, surface and dielectric behavior**

Peksa, Anna; Wolf, Karl-Heinz; Slob, Evert; Chmura, Lukasz; Zitha, Pacelli

**DOI**

[10.1016/j.petrol.2016.10.024](https://doi.org/10.1016/j.petrol.2016.10.024)

**Publication date**

2016

**Document Version**

Final published version

**Published in**

Journal of Petroleum Science and Engineering

**Citation (APA)**

Peksa, A., Wolf, K.-H., Slob, E., Chmura, L., & Zitha, P. (2016). Original and pyrometamorphical altered Bentheimer sandstone: Petrophysical properties, surface and dielectric behavior. *Journal of Petroleum Science and Engineering*, 149, 270-280. <https://doi.org/10.1016/j.petrol.2016.10.024>

**Important note**

To cite this publication, please use the final published version (if applicable).  
Please check the document version above.

**Copyright**

Other than for strictly personal use, it is not permitted to download, forward or distribute the text or part of it, without the consent of the author(s) and/or copyright holder(s), unless the work is under an open content license such as Creative Commons.

**Takedown policy**

Please contact us and provide details if you believe this document breaches copyrights.  
We will remove access to the work immediately and investigate your claim.



## Original and pyrometamorphical altered Bentheimer sandstone; petrophysical properties, surface and dielectric behavior



Anna E. Peksa<sup>a,\*</sup>, Karl-Heinz A.A. Wolf<sup>a</sup>, Evert C. Slob<sup>a</sup>, Łukasz Chmura<sup>b,1</sup>, Pacelli L.J. Zitha<sup>a</sup>

<sup>a</sup> Delft University of Technology, Geoscience & Engineering, Stevinweg 1, 2628 CN Delft, The Netherlands

<sup>b</sup> Royal Smit Transformers B.V., Groenestraat 336, 6531 JC Nijmegen, The Netherlands

### ARTICLE INFO

#### Keywords:

Bentheimer sandstone  
X-ray diffraction  
Thermogravimetry and differential scanning calorimetry  
Firing  
Surface charge  
Permittivity

### ABSTRACT

Bentheimer sandstone is a quartz-rich permeable hard sedimentary rock used for core flooding experiments. When fired to stabilize clays (subjected to high temperatures), pyrometamorphical phase changes induce texture and pore framework alteration. As a consequence the new dielectric response may influence wettability. The literature regarding pyrometamorphical behavior during and after thermal treatment is ambiguous, so we evaluate desirable effects (fixation of clay minerals) and undesirable effects (dielectric surface changes) in the matrix. Porosity, permeability, surface charge, specific surface area and dielectric respond were measured before and after firing of samples up to ~1000 °C under oxidizing and non-oxidizing conditions. The matrix properties were determined using X-ray diffraction and X-ray fluorescence, scanning electron microscope imaging, and thermomechanical-, and thermogravimetric analysis with differential scanning calorimetry.

Firing causes dehydration, dehydroxylation and irreversible transformation of original clays, organic matter, and carbonates to glass, oxides and feldspars. During heating quartz transfers from  $\alpha$ - to  $\beta$ -quartz and back during cooling. This changes the grain volumes and consequently reduces the matrix integrity. The sandstone has a slight porosity and permeability increase (~5%). Further, a shift in the point of zero charge toward a higher pH may result in wettability alteration from strongly water-wet to oil-wet. Additionally, a decrease in the permittivity value and marginal dispersion of the dielectric constant (~5%) between the high and the low frequencies was observed. Due to firing and related dispersion of the iron oxides within the matrix framework, Bentheimer sandstone becomes a weaker insulator.

### 1. Introduction

Bentheimer sandstone (BS) is widely used as a model rock for studying fluid flow in porous media and preparing 3D pore pore-network models for theoretical studies (De Boever et al., 2013; Klein and Reuschlé, 2003; Ruedrich and Siegesmund, 2007). It is an easy to obtain, inexpensive sample material that has a matrix composed of well-sorted, mostly rounded to sub-rounded grains with a regular distribution of pore bodies and pore throats diameter (Peksa et al., 2015). The presence of accessory clay, organic matter and oxides or hydroxides is often ignored. Nevertheless, they influence petrophysical behavior such as permeability and electrical conductivity behavior.

#### 1.1. Motivations for firing

Sandstone samples are heated to temperatures exceeding 500 °C as a common step in core preparations to limit the risk of permeability

reduction during displacement experiments (Potts and Kuehne, 1988; Sydansk). The objective is to remove the chemically bounded water and to transform and stabilize clays. A strong influence of clays in contact with water on sandstone porosity/permeability, pore size geometry and electrical behavior was reported in the literature (Al-Mjeni et al.; Civan and Knapp, 1987; Gabriel and Inamdar, 1983; Gray and Rex, 1966; Huntley, 1986; Klimentos and McCann, 1990; Neasham, 1977; Sharma and Yortsos, 1987; Wildenschild et al., 1999). The high cation exchange capacity of clays, the large surface area and strong interaction with interstitial fluids result in swelling and/or migration. In addition, permeability reduction can be expected because of pore clogging downstream, which causes serious injectivity problems (Gray and Rex, 1966; Jones; Mohan and Fogler, 1997; Mohan et al., 1993; Norrish, 1954). Clay migration was even found to clog high permeable sandstones (>0.5Darcy) (Gray and Rex, 1966). Note that besides clay fines, other components such as organic matter, very fine quartz and feldspars particles, are considered as mobile fines.

\* Corresponding author.

E-mail address: [a.e.peksa@tudelft.nl](mailto:a.e.peksa@tudelft.nl) (A.E. Peksa).

<sup>1</sup> Formerly Delft University of Technology, DC Systems, Energy Conversion & Storage; Electrical Sustainable Energy Department; Mekelweg 4, 628 CD Delft, The Netherlands.

**Nomenclature**

$\alpha$	Average coefficient of expansion, [-]	$S_s$	Specific surface, m/m <sup>2</sup>
$A$	Effective area of the electrode, mm <sup>2</sup>	$\sigma_0$	Charge, C/m <sup>2</sup>
$\Delta\epsilon_r$	Dielectric dispersion magnitude	$\sigma$	Electrical conductivity, S/m
$\Delta n$	Dissolution rate, mmol	$T$	Temperature, °C
$C_0$	Capacitance of space in a parallel-plate capacitor, pF	$t_p$	Polarization duration, min
$C_s$	Capacitance of dielectric in a parallel-plate capacitor, pF	$\tan\delta$	Dissipation factor, [dimensionless]
DAR	Dielectric Absorption Ratio, [-]	$\tan\delta_{pot}$	Polarization losses on the dielectric, [dimensionless]
$\epsilon^*$	Complex electric permittivity in the frequency domain, F/m	$\tan\delta_{cond}$	Conduction losses on the dielectric, [dimensionless]
$\epsilon_0$	Permittivity of space, $\epsilon_0 = 8.85 \times 10^{-12}$ F/m	$U$	Voltage, V
$\epsilon'$	Real part of the electric permittivity, F/m	$V_m$	Matrix volume, m <sup>3</sup>
$\epsilon''$	Imaginary part of the electric permittivity, F/m	$\omega$	Angular frequency, Hz
$\epsilon_r$	Real value of the relative permittivity, [-]		Abbreviations
$\epsilon_{r,r}$	Imaginary value of the relative permittivity, [-]	AC	Alternating current
<b>E</b>	Electric field vector, V·m <sup>-1</sup>	Ant-Rt	Rutile formed as a result of the polymorphic transformation of anatase
$f$	Frequency, Hz	BET	Brunauer-Emmett-Teller
$F$	Faraday constant, C/mol	BS	Bentheimer sandstone
$G$	Conduction, S	CTE	Coefficient of thermal expansion
$G_{AC}$	AC conduction, S	CT	Computed tomography
$G_{DC}$	DC conduction, S	D	Dimension
$g(t)$	Dielectric response function of Bentheimer sandstone sample	DC	Direct current
<b>I</b>	Total current density vector, A/m <sup>2</sup>	DSC	Differential Scanning Calorimetry
$I$	Electric current, A	F	Fired samples
$I_C$	Capacitive part of the current density vector, A/m <sup>2</sup>	Fsp	Feldspar
$I_C$	Capacitive part of the electric current, A	G	Glass
$I_L$	Leakage part of the current density vector, A/m <sup>2</sup>	$H^+$	Hydrogen ion
$I_L$	Leakage part of the electric current, A	Kln	Kaolinite
$I_p$	Polarization current through the sample, A	M	Molar concentration
$I_r$	Insulation resistance, $\Omega$	Mul	Mulite
$L$	Sample length, mm	PZC	Point of zero charge
$L_0$	Initial sample length, mm	Qtz	Quartz
$(\delta L/\delta T)$	Slope of the expansion curve at the temperature, mm/°C	Rt	Rutile
$M$	Mass, g	SEM	Scanning Electron Microscope
$P$	Polarization, C/m <sup>2</sup>	SOL	Dissolution
PI	Polarization index, [dimensionless]	TGA	Thermogravimetric analysis
$\varphi$	Effective porosity, [dimensionless]	UF	Unfired samples
$\rho$	Bulk density, kg/m <sup>3</sup>	WL	Wave length
$R$	Lossy part of the dielectric, $\Omega$	wt%	Weight percent
$\tau_r$	Relaxation time, s	XRD	X-ray diffraction
		XRF	X-ray fluorescence

**1.2. Firing controls on wettability**

Firing of the sandstone caused disintegration of clay minerals, a partial transformation of feldspar and quartz into glass and iron oxides. Moreover, according to Barclay and Worden (2009), if the specific surface of the iron oxides increases, a positive correlation of oil-wetting iron mineral content in the sandstones is observed. González and Moreira (1991) reported iron oxides to be strongly oil-wet due to substantial adsorption of asphaltenes. They observed a significantly higher maximum of asphaltenes adsorption for hematite than for clay minerals (up to 1.5 times) (González and Moreira, 1991). According to Wang and Guidry (1994), the mechanisms of the strong oil-wetness of iron oxides can be explained by (1) ferric ions, allocated on the mineral surface. They represent possible adsorption sites for carboxylic acid anions which can change the wettability of the mineral surface; (2) ferric ions, mainly on the surfaces. They can cause oxidation of the petroleum components using catalysts and produce polar wettability-altering compounds; (3) ferric ions in solution. They may behave as bridges between petroleum and a silica surface. In addition, it must be noted that the wettability state of the reservoirs containing ferric ions ( $Fe^{3+}$ ) is indirectly controlled by the chemistry i.e. redox state, of the

reservoir fluids (Barclay and Worden, 2009).

**1.3. Firing characterization**

Following previous studies (Ma and Morrow, Shaw et al.; Wu and Firoozabadi, 2010) that high temperatures cause changes in mineralogical composition of sandstones and in physical and electrical properties, we decided to fire the Bentheimer samples to temperatures where all silica and carbonate minerals but quartz are dehydrated, dehydroxylized, decarbonized and disintegrated. For Bentheimer sandstone, the information on pyrometamorphical and electrical properties has been found available in the literature is rather limited (Loahardjo et al., 2012; Maloney et al., 1990; Olafuyi et al., 2010). In particular we are not aware of published works on the role of high-temperature minerals, resistive to chemical weathering, within its framework after firing and their effect on wettability. To fill the gap in the understanding of these systems, we decided to perform a series of thermal treatment at temperatures  $\geq 600$  °C and petrophysical, petrological and dielectric experiments.

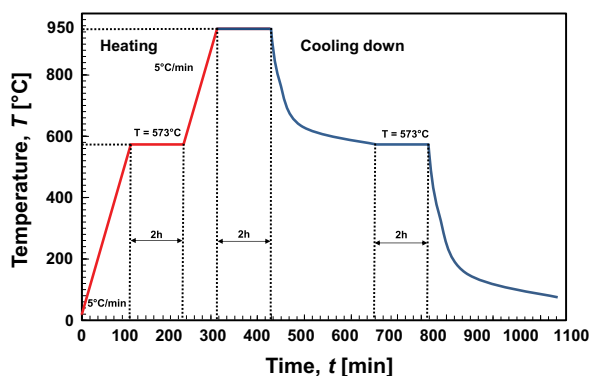


Fig. 1. Temperature path for the firing process of Bentheimer sandstone.

#### 1.4. Electrical behavior

Clay minerals are an important source of ions in the sandstones (Leroy and Revil, 2004; Ma and Morrow; Mohan and Fogler, 1997; Schramm et al., 1991). In our previous study (Peksa et al., 2015), we concluded that iron oxides also influence the surface charge response of the sandstone. Therefore, we decided to perform a series of potentiometric titration experiments to determine the influence of firing on the surface charge. In addition, we performed a thermo-physical analysis of fired and unfired samples, by measuring the dielectric properties in the frequency and time domain. Knowing these properties is important in evaluating the influence of the firing process, as they are related to the constituent materials and the geometrical microstructure of the rock.

The results of this study should help experimentalists in planning combined flow and electrokinetic experiments with Bentheimer sandstone. This article starts with experimental methods, followed by results and discussions; and conclusions.

## 2. Materials and methods

### 2.1. Firing

Sample material placed in a temperature-programmable furnace was heated at atmospheric pressure at a rate of 5 °C/min, up to 573 °C. This temperature was maintained for 2 h for the mineral transformation of  $\alpha$ - to  $\beta$ -quartz. Then, the samples were heated further at the same thermal rate up to 970 °C, where the temperature again was maintained for 2 h. Thereafter, the samples were cooled down by setting the temperature to 573 °C, and again kept for 2 h stabilization at 573 °C, followed by another cool down to room temperature (Fig. 1). The aim of this procedure was to limit thermal shock effects that may cause differential expansion and contraction, that would lead to microfracturing in grains and cracking of grain contacts.

### 2.2. Characterization of unfired and fired samples and thermal analysis

#### 2.2.1. X-ray diffraction (XRD)/X-ray fluorescence (XRF) and texture composition

Samples characterized for XRD and XRF analysis were pulverized to a powder with a particle size of less than 2  $\mu$ m and analyzed for their mineral composition and element-oxide distribution. The XRD was recorded in a Bragg-Brentano geometry, with a Bruker D5005<sup>TM</sup> diffractometer equipped with a Huber incident beam monochromator and Braun PSD<sup>TM</sup> detector. The XRF measurements were conducted with a Panalytical Axios Max WD-XRF<sup>TM</sup> spectrometer measuring the element oxides and elements (>0.5 wt%) with an accuracy of 2%. Details on XRD and XRF and corresponding setups are provided in literature (Morse, 2013; Moore and Reynolds, 1989).

#### 2.2.2. Scanning electron microscope (SEM)

To identify changes in the matrix structure, selected samples were examined using a scanning electron microscope (JEOL 8800 M JXA Super probe<sup>TM</sup>). The methodology of SEM and further image analysis can be found elsewhere (Kransley et al., 2005).

#### 2.2.3. Porosity and permeability measurements

Porosity and permeability were determined on cylindrical samples having a diameter of 30 mm and length of 36 mm. Dry porosity tests were conducted with a Gas Expansion UltraPycnometer 1000 (Quantachrome Instruments<sup>TM</sup>) using Boyles's gas expansion law (Selley and Sonnenberg, 2014). The results are the matrix volume ( $V_m$ ), the bulk density ( $\rho$ ) and the porosity ( $\phi$ ). The permeability of dry cores was measured with N<sub>2</sub> gas by using a Ruska gas permeameter (Ruska Instruments<sup>TM</sup>) (Tiab and Donaldson, 2015).

#### 2.2.4. Thermogravimetry (TGA) and differential scanning calorimetry analysis (DSC)

For thermal analysis, the samples were crushed to powders with particles smaller than 50  $\mu$ m. The thermos-analyzer Netzsch STA F3 Jupiter<sup>TM</sup> with QMS403C Aëolos<sup>TM</sup> gas analysis system was simultaneously used to conduct thermogravimetric analysis (mass change  $\pm$  1  $\mu$ g) and differential scanning calorimetry (heat difference  $\pm$  0.1  $\mu$ W). The instrument measures the mass changes and provides endo-/exothermic results as a function of temperature against a reference measurement in an empty crucible (Gabbott, 2008). The measurements were performed in both argon and air conditions at atmospheric pressure. The standard firing procedure was done in the air atmosphere, although to acquire more information about thermal mineral behavior in a neutral or reducing environment, argon was introduced. The gas velocities were 20 ml/min, with a dynamic temperature program at rate of 10 °C/min. In order to detect possible drying of the sample, the measurement started at 30 °C and went to a maximum temperature of  $\sim$ 1000 °C ( $\pm$  1.5 °C).

#### 2.2.5. Thermal expansion

To measure the changes in the physical properties of sandstone such as coefficient of thermal expansion ( $\alpha$ ) and linear thermal expansion ( $\Delta L/L$ ), mechanical analysis techniques in thermal analysis were used (Haines, 2002). The cuboid sample of 5.34 mm  $\pm$  0.01 mm in length and of a cross-sectional area 4 mm x 4 mm was placed in the PerkinElmer<sup>TM</sup> thermomechanical analyzer to measure small changes in sample dimensions. The sample was evenly heated over a programmed temperature range of 10 °C/min up to maximum 600 °C and kept constant for 2 h. Thereafter, it was cooled down at the same rate. The thermomechanical analyzer converts movements of the probe into an electrical signal and generates the thermal response curves from which the coefficient of thermal expansion was derived. The average coefficient of thermal expansion (CTE) is represented by  $\alpha$ , that is a function of temperature:

$$\alpha(T) = \frac{1}{L_0} \left( \frac{\partial L}{\partial T} \right), \quad (1)$$

where  $\left( \frac{\partial L}{\partial T} \right)$  is the change in the sample length ( $L$ ) over a temperature range expressed as a slope of the expansion curve at temperature  $T$ ;  $L_0$  is the initial sample length.

#### 2.2.6. Surface charge and specific surface area

Potentiometric titrations were performed in a nitrogen atmosphere to the change in surface charge of Bentheimer sandstone due to the firing process. Before starting the experiments a sample of Bentheimer (0.5, 5 and 10 g) was dispersed in the electrolyte (100 ml H<sub>2</sub>O with 9 ml of 0.1 M NaOH) and then stirred vigorously with a Teflon magnetic stirrer for 24 h. The potentiometric titrations were performed by adding 0.1 M HCl droplet by droplet, while continuously stirring the

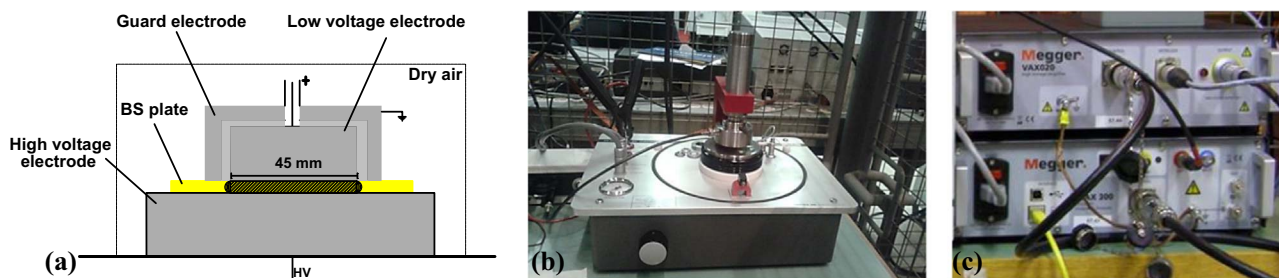


Fig. 2. (a) Schematic of the three-terminal parallel-plate capacitor, showing the high voltage electrode at the bottom and the low voltage electrode surrounded by the guard electrode at the top; (b) the electrode terminal; (c) Megger<sup>TMM</sup> device for capacity measurements at atmospheric conditions.

solution. The pH data were recorded every 5 min. The pH-dependent surface charge ( $\sigma_0$ ) was calculated as Janusz (1999):

$$\sigma_0(pH) = - \frac{F \cdot (\Delta n_{sol,H^+}(pH) - \Delta n_0)}{M a_s} = \frac{f_{surf}(pH)}{S_s}, \quad (2)$$

where  $F$  is the Faraday constant ( $F=96500$  C/mol);  $M$  is sample mass;  $S_s$  surface area and  $\Delta n_0$  the pH-dependent amount of acid/base consumed. The dissolution effect ( $\Delta n_{sol,H^+}$ ) was obtained by comparison of the balance of protons and hydroxyl ions in the potentiometric titration of Bentheimer samples with blank potentiometric titration results:

$$\Delta n_{sol,H^+}(pH) = \Delta n_{acid\backslash base(BS)}(pH) - \Delta n_{acid\backslash base(blank)}(pH). \quad (3)$$

For correct interpretation of the electrical behavior of the powdered fresh and fired Bentheimer sandstone, the specific surface area was measured by adsorption of liquid nitrogen, at low temperatures ( $-196.5$  °C). The detailed methodology is provided elsewhere (Peksa et al., 2015). The specific surface data was calculated using the BET sorption theory (Brunauer et al., 1938). The obtained specific surface area represents the “external” surface area, since the penetration through the interlayer of smaller clay particles surfaces by weakly adsorbed nitrogen is not entirely possible.

### 2.3. Dielectric spectroscopy

#### 2.3.1. Principle and apparatus

The main objective of the dielectric spectroscopy studies was to study differences in between unfired and fired samples through the frequency dependence of the permittivity and dissipation factor. The secondary objective is to conduct the dielectric adsorption test under DC conditions to recognize a change in the conductive behavior. For the tests, flat circular discs with a diameter  $d$  of 140 mm and thickness,  $h$  of 8–10 mm were placed between two electrodes to arrange a parallel-plate capacitor of plate area,  $A \sim 15.9 \cdot 10^2$  mm<sup>2</sup>. The contact surface of the samples and the electrodes was sufficiently smooth for the current transfer to occur.

The apparatus used for the measurement of the dielectric properties of the samples consists was a three-terminal parallel-plate capacitor connected to a Megger<sup>TMM</sup> capacity meter (Fig. 2) consisting of: (1) a bottom electrode directly connected to a high voltage unit, and (2) a top electrode connected to a low voltage terminal. The internal part of the upper electrode is used for measurements while the external part acts as a guard and eliminates the influence of surface leakage currents from the measurement results (Fig. 2a). The electrode terminal is covered by a tight glass shade to prevent the entrance of moisture from the atmosphere.

#### 2.3.2. Sample preparation

Prior to the experiments, several techniques are employed to remove the water including heating in the oven at 105 °C for 48 h, and further saturation of the cores placed in the three-terminal

parallel-plate capacitor with dry air. The drying procedure in the capacitor was implemented three times for each sample. Samples were subsequently: saturated with 90 °C dry air, evacuated, re-saturated with dry air, and then stored in a dry air atmosphere for 24 h. Measurements were later made with the cores in vacuum. The above procedure ensured the removal of free water from the samples. To reduce and quantify the effect of the electrode polarization (ionic charge accumulations at the electrodes) (Ishai et al., 2013) the following methods have been used when measuring dielectric properties: (1) varying the thickness of the samples to quantify the polarization effect; (2) using aluminum films as spacers to reduce the effect as much as possible.

#### 2.3.3. Dielectric permittivity test

The test cell was connected to a capacity meter that measures the capacity and the dissipation factor of a sample as a function of frequency at a desired voltage of  $U=0.5$  kV. A non-ideal dielectric like BS supports a varying charge, adsorbs and dissipates the electric energy in the form of heat. When a potential difference is applied to a capacitor, energy is dissipation dissipated due to two main factors: (1) a flow of free charges through the material, called conduction loss (DC term), and (2) a displacement of electric charges that gives rise to the creation of dipoles in the sample (AC term). The second mechanism, called polarization  $P$ , arises as a result of an electronic and an ionic polarization, a dipole orientation and an interfacial polarization (Howell and Licastro, 1961). The polarization of heterogeneous materials like Bentheimer sandstone depends on the individual properties of minerals, their proportion and distribution across the sample volume. This mechanism is related to the space charge accumulation along the interface in the presence of the electrical field. For this reason, it can be expected that the relative permittivity of a mixture of minerals may exceed that of a single mineral. Different types of polarization have varying time response abilities to an applied field

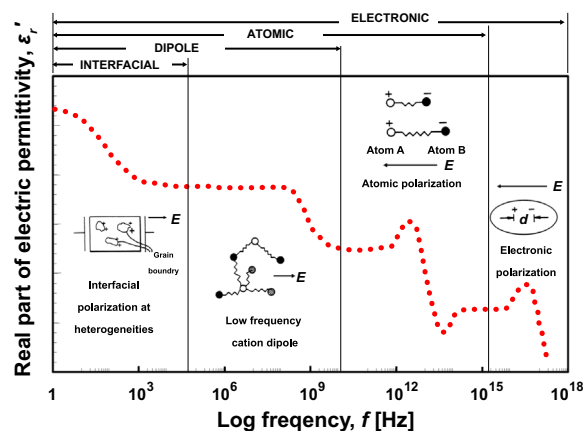
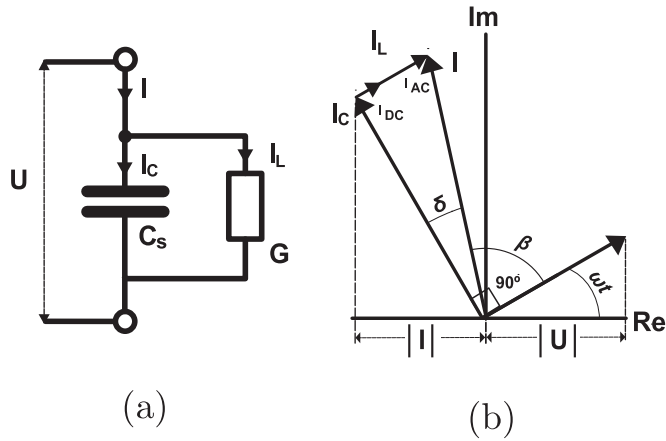


Fig. 3. The real part of electric permittivity spectrum over a range of frequencies (Izgorodina et al., 2009).



**Fig. 4.** (a) Schematic of the parallel equivalent circuit. Note that it corresponds to one voltage and frequency level; (b) corresponding phasor diagram representing the electric loss angle  $\delta$ , and power factor angle  $\beta$ . As a result of the introduced voltage  $U$ , the current  $I_L$  follows in phase with the applied voltage, and the charging current  $I_C$  is  $\pi/2$  out of phase.

frequency. Therefore, the real part of electric permittivity is frequency dependent (Fig. 3). The frequency dependence of the polarization process on the relative permittivity value is presented elsewhere in greater detail (Dakin, 2006). Measurements conducted that are described in this paper cover the interval of the frequency domain from 0.1 to 15 kHz. Application of an electric field  $E$  gives rise to the electric displacement field  $D$  flowing the relation (Laj and Channell, 2007):

$$D = \epsilon^* E. \tag{4}$$

The interactions of a material with an electric field  $E$  are described by the complex electric permittivity  $\epsilon^*$ :

$$\epsilon^* = \epsilon' - i\epsilon'', \tag{5}$$

where the expressions  $\epsilon'$  and  $\epsilon''$  define the real and non-negative component of the permittivity and the energy dissipation due to polarization, respectively. The real part of the complex permittivity can be calculated at the various frequencies by using the measured capacitance values of a sample in a parallel-plate capacitor between the high and low voltage electrode ( $C_s$ ) at the strong accumulation region from the relation (Bartnikas, 1987)

$$C_s = \epsilon_r C_0, \tag{6}$$

where  $C_0$  is the capacitance without the sample,  $\epsilon_r$  denotes the real part of the relative permittivity, represented by the ratio  $\epsilon_r/\epsilon_0$ , where  $\epsilon_0$  is the permittivity in vacuum.

Due to the existence of the loss current, the BS in the parallel-plate capacitor can be defined as a “leaky” dielectric and can be represented by the equivalent circuit (Fig. 4a). The losses in the sample can be represented by a conductance  $G$ . If an AC voltage source  $U$  is applied on the capacitor, the total current  $I$  propagating in the sample consists of two components:

$$I = I_C + I_L. \tag{7}$$

A charging current  $I_C$  leads the in-phase component current by  $90^\circ$  (Fig. 4b) and can be expressed by

$$I_C = \omega C_s U, \tag{8}$$

where  $\omega$  denotes the angular frequency ( $\omega = 2\pi f$ ). A loss current  $I_L$  that is in phase with the applied voltage includes the AC conduction from the inertial resistance  $G(\omega)_{AC}$  and the DC conduction  $G_{DC}$

$$I_L = (G(\omega)_{AC} + G_{DC})U \tag{9}$$

$$\text{with } G(\omega)_{AC} = \omega C_0. \tag{10}$$

The DC conductance  $G_{DC}$  of the samples can be represented in

terms of the electrical conductivity  $\sigma$  as  $G_{DC} = \sigma A/d$ . Thus, implementing (8), (9) and (10) into (7), the total current for a BS sample can be expressed as

$$I = (i\omega\epsilon_r C_0 + \omega\epsilon_{nr} C_0 + G_{DC})U = ((i\omega C_0)\epsilon_r^* + G_{DC})U \tag{11}$$

where  $\epsilon_{nr}$  is the imaginary value of the relative permittivity, represented by  $\epsilon_{nr}/\epsilon_0$  ratio. From the above expressions and from the parallel circuit presented in Figs. 4a and b, the total dissipation factor value of the sample can be derived as Arora and Mosch (2011), Nabighian (1987)

$$\tan\delta = \frac{I_L}{I_C} = \frac{G_{DC} + \omega\epsilon_{nr} C_0}{\omega\epsilon_r C_0} = \frac{G_{DC}}{\omega\epsilon_r C_0} + \frac{\epsilon_{nr}}{\epsilon_r}. \tag{12}$$

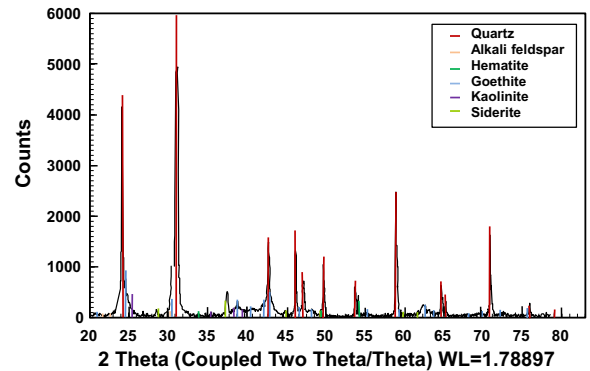
The total dissipation factor of a dielectric is characterized by the sum of: a) the polarization losses,  $\tan\delta_{pol}$ , and b) the losses caused by conduction,  $\tan\delta_{cond}$  when the resistance of the dielectric is sufficiently small. Hence, the dissipation factors related to the polarization and conduction are equal to:

$$\tan\delta_{pol} = \frac{\epsilon_{nr}}{\epsilon_r} = \frac{\epsilon''}{\epsilon'}, \tag{13}$$

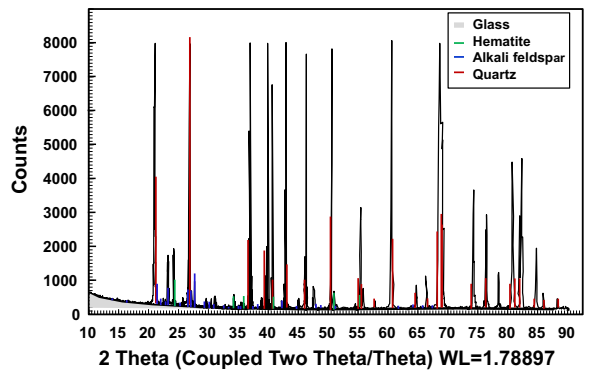
$$\tan\delta_{cond} = \frac{\sigma}{\omega\epsilon_0\epsilon_r}. \tag{14}$$

Assuming that the DC contribution of loss current is much smaller than the AC contributions ( $G_{DC} \ll \omega\epsilon_{nr} C_0$ ), the total dissipation factor simplifies to

$$\tan\delta = \frac{\epsilon''}{\epsilon'}. \tag{15}$$



(a)



(b)

**Fig. 5.** XRD pattern of (a) the unfired Bentheimer sandstone sample; (b) the fired Bentheimer sandstone sample.

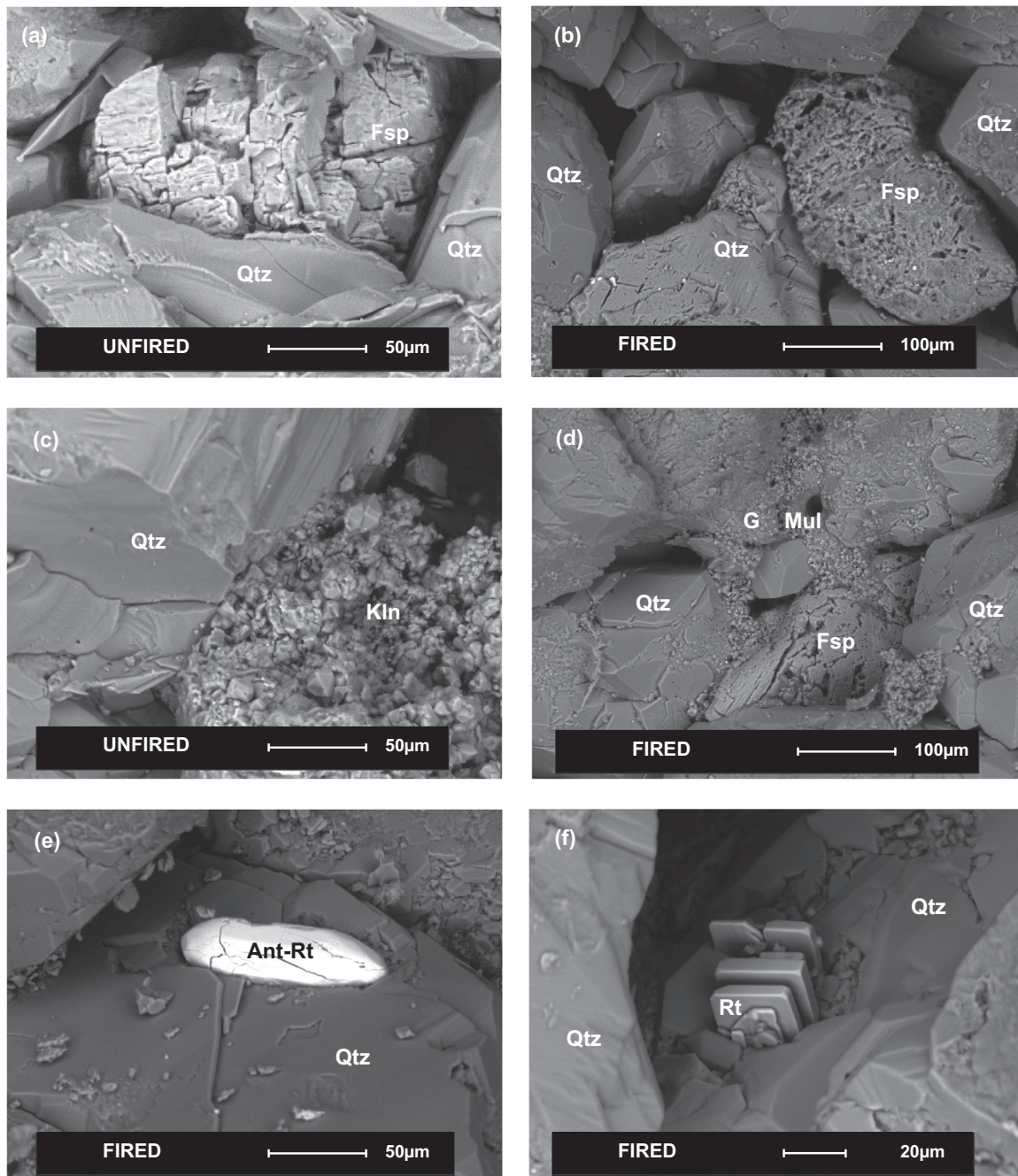


**Fig. 6.** Scanning electron microscope (SEM) image of: (a) original quartz (Qtz), lower right see the quartz overgrowth and alkaline feldspar (Fsp); (b) thermally affected quartz grain (Qtz) and a deteriorated feldspar (Fsp) with discrete interfaces between the grains; (c) kaolinite (Kln) and quartz (Qtz) grain in unfired samples; (d) glass-like regions (G) formed as an occurrence of clays vitrification. The deteriorated feldspar grain (Fsp), metakaolin and initial formation of mullite (Mul) formation are observed; (e) rutile formed as a result of the polymorphic transformation of anatase (Ant-Rt); (f) rutile in a form of accessory precursor phase (Rt).

**2.3.4. Polarization current measurements and dielectric absorption test**

The main concept of this test is the increase in insulation resistance due to the polarization of the atoms in sandstone over time. The DC voltage ( $U=0.2$  kV) is applied to samples placed in the same three-terminal parallel-plate capacitor during a polarization duration,  $t_p > 10$  minutes. Thus, due to the application of a DC voltage  $U$ , a pulse-like polarization current flows through the sample. During the polarization duration, the current decreases to a certain value corresponding to the conduction current. This is assuming that the sample in the parallel-plate capacitor is totally discharged prior to the measurement and that a step voltage is applied with the following characteristics (Jonscher, 1984)

$$U(t) = \begin{cases} 0 & t < 0 \\ U_0 & 0 \leq t \leq t_p \\ 0 & t > t_p \end{cases} \tag{16}$$

The above relation gives zero current for times before  $t=0$ , and polarization currents for times  $0 \leq t \leq t_p$ . The polarization current through the sample can be expressed as Jonscher (1984)

$$I_p = U_0 C_0 \left[ \frac{\sigma}{\epsilon_0} + \epsilon_\infty \gamma(t) + g(t) \right], \tag{17}$$

It contains three parts: (1) process independent of any polarization being in relation to the conductivity of the sample; (2) the gamma function, arising from the suddenly applied step voltage, at  $t=0$  and

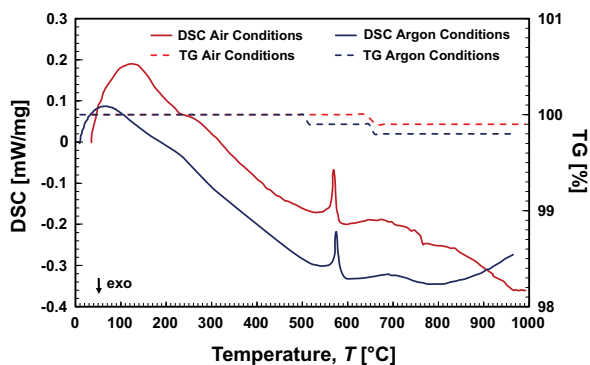


Fig. 7. Thermogravimetry and differential scanning calorimetry analysis of Bentheimer sandstone under the air and argon atmosphere, at heating rate 10 °C/min.

$t=tp$ . A large dynamic range of current amplitudes related to the sudden polarization processes makes this term ignored in the calculation; (3) the activation process of the certain polarization within the sample,  $g(t)$ . Therefore, (17) can be rewritten as

$$I_p = U_0 C_0 \left[ \frac{\sigma}{\epsilon_0} + g(t) \right], \quad (18)$$

NOTE: The dimension of  $g(t)$  is 1/s and its magnitude is tied to  $C_0$ . Moreover, the simultaneous measurements of the insulation resistance ( $I_r$ ) at different time intervals allow the calculation of: a) dielectric absorption ratio (DAR) that is the ratio of the insulation resistance at 60 s to the insulation resistance at 30 s, and b) the polarization index (PI) that is the ratio of the insulation resistance value measured at 600 s to the insulation resistance value measured at 60 s. All reported polarization current measurements were performed at ambient temperature.

### 3. Results and discussion

#### 3.1. XRD/XRF analysis and SEM interpretation: general results

The pyrometamorphic alterations up to 970 °C have been evaluated by XRD/XRF-analysis and SEM. The primary constituents of the Bentheimer sandstone are quartz (91.7 wt%), feldspars (4.9 wt%), clay minerals (2.7 wt%), carbonates (0.4 wt%), pyrite and iron hydroxides (0.2 wt%). Note that the wt% are average values from the analysis of our previous study (Peksa et al., 2015). Additionally, SEM analyses show the presence of kaolinite, illite, and mixed-layer clays in Bentheimer sandstone.

Fig. 5 mainly shows the reduction of intensity corresponding to kaolinite in the XRD patterns between unfired and fired Bentheimer sandstone. In samples fired to 970 °C the structure became amorphous, and might only represent traces of meta-kaolinite and mullite (Figs. 6c–d) (Friolo et al., 2005; Ismailov, 1981). Quartz and feldspars were transformed to a lesser extent in comparison to other components, as most of the sandstone components have a lower melting point than quartz. They melt first creating vitrified textures and consequently, the quartz grains dissolve into the glassy matrix (Figs. 6c–d). In the case of the feldspar grains, a disappearance of clay minerals is observed. It results in irregular grain shapes, and in small amounts of glass at the grain boundaries (Fig. 6d). Therefore, it indicates an initial integration of the feldspars into melts. Moreover, distinct interfaces between the grains were recognized in the SEM-photos (Fig. 6b). Before firing, the boundary between the detrital quartz grains was merged by overgrowths and/or pressure solutions.

Furthermore, hematite was identified as a minor component in the unfired sample and as well in an increased amount as a secondary phase. Decomposition of most of iron (hydro) oxides/carbonates (goethite, siderite) and iron rich cement resulted in conversion to

mainly hematite and probably wüstite, giving the rock a distinctive reddish color (supplement Fig. S1). The destruction of the cementing material by firing made Bentheimer more friable. An interesting observation was SEM identification of rutile as an accessory component, occurring both as a precursor and as a polymorph phase after anatase (Figs. 6e–f).

#### 3.2. Thermal analysis and phase transformations

TGA and DSC analyses were carried out in argon and air environment, and the results are illustrated in Fig. 7. The dehydration of sandstone components is observed in the DSC traces with an initial endothermic peak observed between 40 °C and 170 °C, and between 20 °C and 90 °C in the air and argon environment, respectively. The process is related to free water being removed from the minerals. In the range 200–350 °C, small endothermic peaks demonstrate the dehydration of iron-oxides and -hydroxides and the crystallization of iron oxide, mainly hematite (Prasad and Sitakara Rao, 1984; Sharma et al., 1994). The slight mass losses observed in the thermal data in the region 470–650 °C in each of the TG curves indicate dehydroxylation processes and thermal decomposition resulting into oxidation in air and reduction with oxygen release in an argon environment. In region 470–650 °C (in each of the DSC curves) peaks centered at 580 °C corresponding to the dehydroxylation of kaolinite are observed (Grim, 1968). For argon atmosphere, an additional endothermic reaction took place above about 750 °C, while endothermic disintegration and exothermic oxidation occurred in the air. In the air environment, the exothermic peak can be associated with mullite formation (Carroll, 1970; Friolo et al., 2005; Ismailov, 1981).

The results of thermal expansion measurements are presented in Figs. 8a and b. It can be observed that the slope is unlikely to be constant, varying from  $10.9 \cdot 10^{-6}/^{\circ}\text{C}$  to  $35.2 \cdot 10^{-6}/^{\circ}\text{C}$  (1–4 boxes in

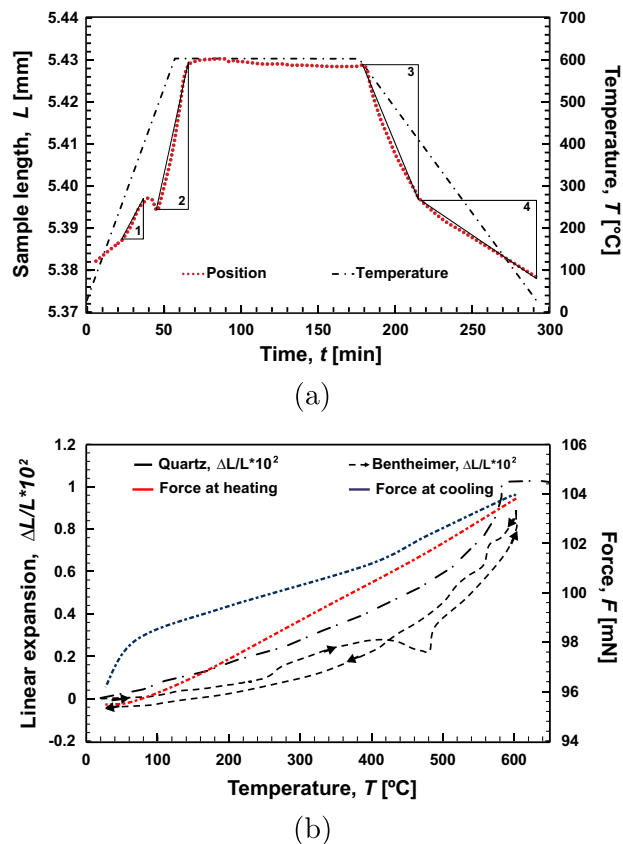


Fig. 8. (a) Thermal expansion ranges: (1)  $10.9 \cdot 10^{-6}/^{\circ}\text{C}$ , (2)  $35.2 \cdot 10^{-6}/^{\circ}\text{C}$ , (3)  $32.9 \cdot 10^{-6}/^{\circ}\text{C}$ , (4)  $15.4 \cdot 10^{-6}/^{\circ}\text{C}$ ; (b) linear thermal expansion of Bentheimer sandstone and quartz (Somerton, 1992) vs. temperature.

**Table 1**  
Thermal behavior of the minerals present in the Bentheimer sandstone after Kühnel (1998) Wolf (2006).

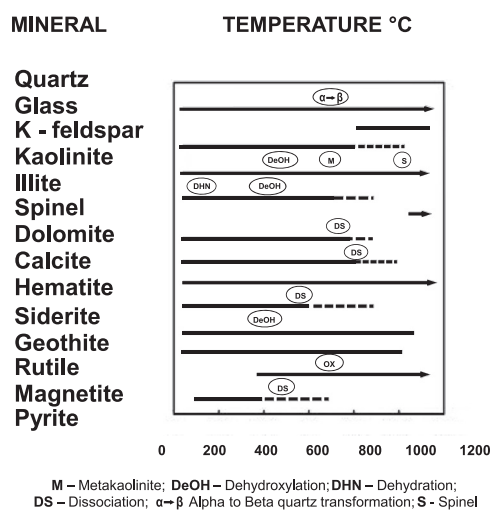


Fig. 8a). The most visible expansion occurs above 500 °C. The structure of the kaolinite breaks down in the endothermic reaction results into meta-kaolinite and a consequent distortion of structures (Fig. 6 and Table 1). Quartz undergoes a trigonal  $\alpha$ -quartz to hexagonal  $\beta$ -quartz transformation and above 800 °C disintegrated feldspars create a vitrified textures with melting illite (Fig. 6d and Table 1). The cooling curve of Bentheimer differs significantly from the heating curve; this difference is due to the elongation of quartz grains during heating.

To a lesser extent, the change in sample length between the beginning and the end of the experiment can be attributed to the greater force acting on the sample at the final stage of the experiment. For comparison, the linear thermal expansion of quartz is included in Fig. 8b. A similarity in the heating curve trend between Bentheimer and quartz is observed. As shown above, the deformation and expansion of the sample is mainly governed by quartz; however, at temperatures above 573 °C (where the transition from  $\alpha$ - to  $\beta$ -quartz occurs), the coefficient becomes negative (Fig. 8b), which suggests that more constituents than quartz control the expansion process in Bentheimer sandstone. The thermal expansion curves prove again that there are no high-temperature forms of quartz.

### 3.3. Porosity and permeability

Permeability and porosity of the Bentheimer Sandstone cores can be expected to vary as a consequence of firing along with texture and mineral alteration. Firstly, a differential thermal expansion may cause cracking of the grain contacts and by that increase of the pore volume. Secondly, the disintegration and recrystallization of minerals that have a lower melting point than quartz may slightly increase the quartz grain volume. As well the differential expansion of minerals separates grains at the interfaces (Fig. 6b) and thus, creates an irreversible volume increase (Kühnel, 1998; Wolf, 2006; Somerton, 1992; Bhargava et al., 2009). Fig. 9 shows that the absolute gas permeability against porosity hardly changed before and after thermal treatment. The porosity and permeability both increased by less than 5%, which is within the experimental error for usual core flood tests. The slight change in the porosity and permeability is most likely due to textural and compositional changes. As stated by Klimentos and McCann (1990) clays, even in small amounts, may strongly influence flow parameters of the rock. Due to exposure to high temperatures ( $\sim 970$  °C), clays undergo

decomposition and degradation, and, as a result, change the sandstone matrix structure. On the other hand quartz undergoes reversible reaction at 573 °C from  $\alpha$ - to  $\beta$ -quartz. That is related to the increasing vibrations and slight displacement of the atoms in the crystal lattice, and further volume increase (Ghiorso et al., 1979). Moreover, the firing process leads to weakening and releasing of the cementing material, which results in dispersion and relocation of fine particles within the sandstone pore matrix (Ma and Morrow).

### 3.4. Surface charge

The potentiometric titration for establishing surface charge behavior was started in alkaline pH ( $>12$ ). Comparing the titrated surface charge curve obtained from fired Bentheimer sandstone samples, Fig. 9b, to unfired (Peksa et al., 2015) shows that protons bind to surfaces at the highest protons affinity sites. Subsequently, with an addition of HCl the sites with lower proton affinity come to be protonated.

For unfired and fired samples the change in the pH value, with addition of 0.1 M HCl titrant, showed a similar trend for the same mass of the samples, however with a steeper gradient for fired samples so that the point of zero charge (PZC) for unfired and fired samples are respectively at pH=8 and pH=10.6. The shift in the PZC can be attributed to a higher concentration of iron oxides present in the sample after firing.

In the Bentheimer sandstone, the iron oxides coatings on quartz grains can give large local specific surface areas. At the low pH, they may reduce a negative charge due to (1) the physical blockage of negative charges by iron oxides coatings on e.g. quartz grains, (2) the mutual neutralization of negatively charged particles (Sumner, 1963). It proves the previous remark that as a result of firing iron becomes grain coating material, which can significantly influence the surface response of the sample. Iron oxides might be strongly oil-wet and result in a change of the wettability of Bentheimer sandstone. Nevertheless, in the terms of the volume, the iron oxides can be neglected.

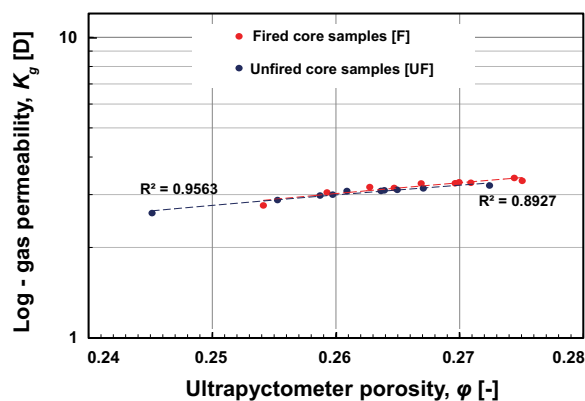
### 3.5. Dielectric spectroscopy

The frequency dependence on the electric parameters for fired and unfired samples was examined at pressure of 2 bars, temperature of 30 °C. The obtained values were compared with predictions made using the model of Lichtenecker and Rother (1931).

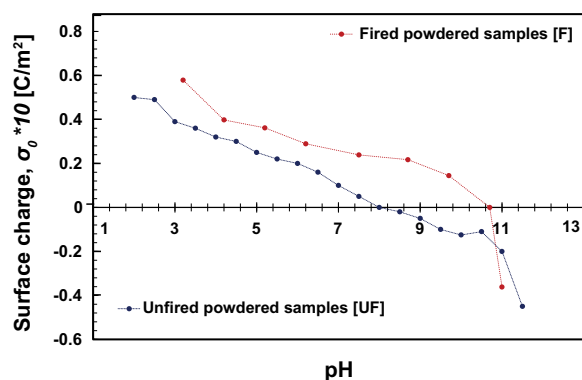
#### 3.5.1. Dielectric permittivity

The variation of the real part of electric permittivity  $\epsilon_r$  and the dissipation factor  $\tan\delta$  as a function of frequency are depicted in Figs. 10a and b. The results represent average values over three consecutive tests. It is observed that the real part of electric permittivity decreases after the samples are thermally treated. Fig. 10a shows that over the frequency range of 0.1–10 Hz where the counter ion diffusion polarization occurs, the dielectric dispersion magnitude is  $\Delta\epsilon_{r,min} = 0.5$  (for sample 13A) and  $\Delta\epsilon_{r,max} = 3.27$  (for sample 12A). It decreases with increasing frequency reaching  $\Delta\epsilon_{r,min} = 0.13$  (for sample 13A) and  $\Delta\epsilon_{r,max} = 0.39$  (for sample 12A) over the frequency range of 10 Hz to 15 kHz. This phenomenon in the low frequency regimes is common for rocks and is attributed to the variation in polarization, being a result of the charge accumulation at the grain boundaries, and/or grain imperfections, and further, the composition heterogeneity in the rock matrix (Saint-Amant and Strangway, 1970; Sengwa and Soni, 2006). This has been explained previously by a Maxwell-Wagner model (Howell and Licastro, 1961). For high frequencies ( $>MHz$ ) this effect will be negligible (Rao and Smakula, 1965).

For the thermally treated samples, the dielectric constants measured at low frequencies are up to  $\sim 5\%$  larger than those at the high frequencies, which is a much smaller variation than that observed in



(a)



(b)

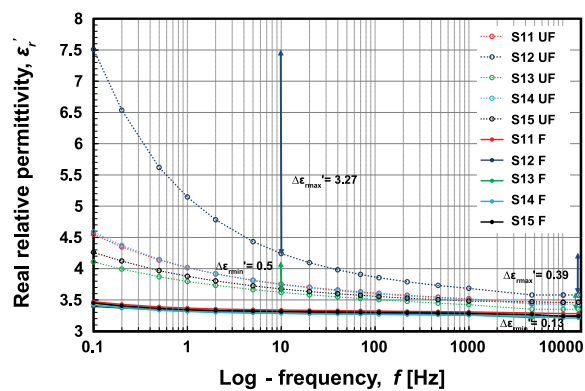
Fig. 9. (a) Por/permeability cross plot for unfired and fired Bentheimer samples; (b) surface charge of fired Bentheimer sandstone.

the unfired samples. Differences in permittivity results between fired and unfired samples are mainly due to the transformations of clay due to firing. The high specific surface area minerals (i.e. clays) usually exhibit higher dielectric dispersion magnitudes than low specific surface area minerals (Arulanandan, 2003). The low dielectric constant value for fired samples that contain iron oxides (the large specific surface and capillary retention capacity) was discussed by Van Dam et al. (2002). They demonstrated that the iron oxides do not directly alter the relative permittivity of the solid phase in the sediment. However, the correlation exists between the larger specific surface and capillary retention capacity of iron oxides, as compared with quartz grains. Thus, iron oxides can have a profound influence on the relative permittivity if they occur in larger quantities than in the Bentheimer sandstone (TGA measurements and XRD).

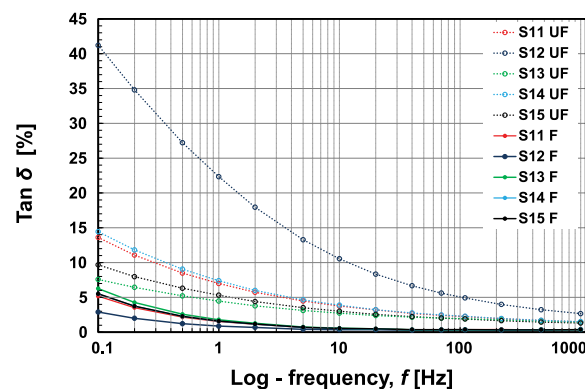
### 3.5.2. Dissipation factor

Fig. 10b shows the dissipation factor vs. frequency. At low frequencies, losses are much higher than at higher frequencies for both fired and unfired samples. For the fired samples, at frequencies larger than 10 Hz, the dissipation factor is almost independent of frequency. This can be explained by a Maxwell-Wagner effect for a widespread distribution of conductivity of the accessory minerals and thermos-mineralogical alterations within Bentheimer (Saint-Amant and Strangway, 1970). With increasing frequency, a slightly different approach that influences the dissipation factor behavior, the Garton's mechanism (Garton, 1941), is observed. More tests in higher frequencies should be conducted to entirely confirm that statement. Note that this mechanism of invariance with frequency is a special case for quartz (Argall and Jonscher, 1968).

The observed general dispersion in the obtained results can be attributed to local heterogeneities due to varying clay concentrations in



(a)



(b)

Fig. 10. (a) The frequency domain dielectric constant spectrum for unfired and fired samples; (b) tangent loss spectrum over the frequencies; S11UF-S15UF corresponds to samples before thermal treatment, and S11F-S15F to samples after firing.

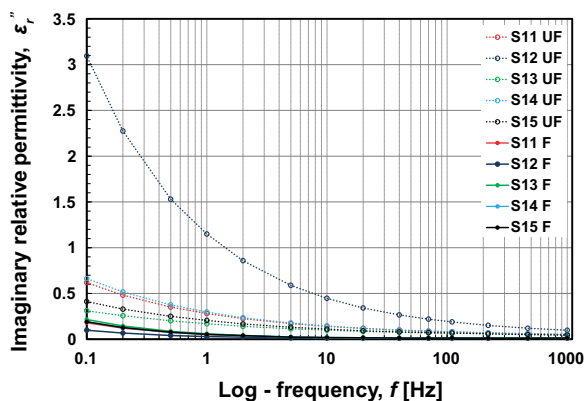
the Bentheimer samples. The variation in the dielectric constant is directly related to differences in the mineral composition, the crystal structure and the relation and interaction of the various constituents of the rocks to one another, besides clay.

The trend of a decrease in dielectric permittivity and the corresponding change in the dielectric properties have been ascertained by the extended drying process and repeated measurements. Attention was taken to eliminate any possible moisture and instrumental source causing variations in the measurements. While conducting the measurements, we found that there is a difference between the results obtained at certain stages of the drying. Hence, the measurements account as “dry rock” were obtained after the third drying when the value of the loss tangent varied <0.5% between repeated measurements. Fig. 11b shows the influence of water content on the dielectric constant of unfired sample no. 14 with different moisture content in the frequency domain covering the interval from 1 Hz to 1 kHz. The trend of spectrum variation is close to the dry rock samples, although a noticeable role of moisture is observed.

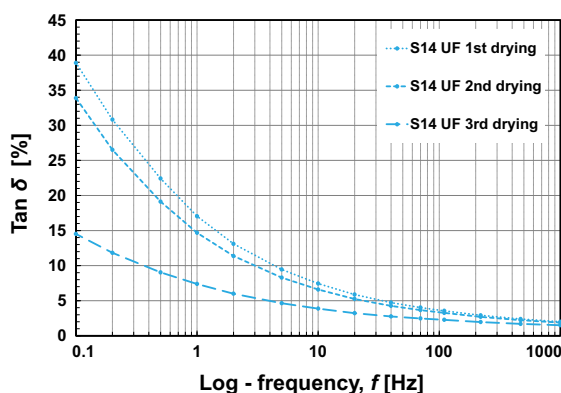
### 3.5.3. Polarization current and the dielectric absorption test

For the dielectric absorption test, the DC voltage  $U=0.2$  kV was used. As a result, a polarization current,  $I_p$ , flows through the dielectric. Subsequently with time, the transient phenomena “polarization current decay” heads to a small steady state conduction current (Fig. 12).

For both samples, the application of a DC electric field results in a current jump as an effect of fast electronic, ionic and orientation polarization. Subsequently, the current decreases gradually due to slow polarization processes. A good fit of the Curie-von Schweidler model (Curie, 1888; Schweidler, 1907) with the measured data was obtained.



(a)



(b)

Fig. 11. (a) The imaginary permittivity spectrum over the logarithm of the range of the frequencies for unfired and fired samples; (b) effect of moisture on the tangent loss value over the logarithm of the range of the frequencies for sample 14UF.

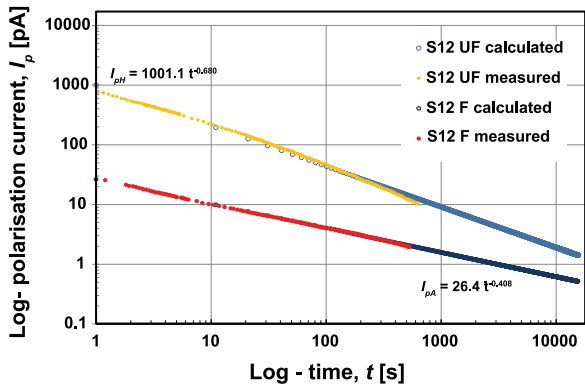


Fig. 12.  $t - I_p$  characteristic of a dielectric after voltage application.

The observed decay phenomena can be described by a power function, where the space charge formation creates an inner electric field of the opposite direction which progressively decreases the current. Fig. 12

Table 2  
The dielectric absorption test results.

Fired samples	Unfired	Fired
Average Insulation Resistance 60 s [TΩ]	15.57	26.35
Average Dielectric Absorption Ratio (DAR)	1.64	1.3
Average Polarization Index (PI)	4.7	2.2
Insulation Condition	Good	Questionable

shows the variation of the polarization current with time and sample treatment (unfired and fired).

The application of DC voltage for fired samples showed that changes in mineral composition and their conductivity tend to affect the tail of polarization currents. Due to firing and related dispersion of the iron oxides within the matrix framework, Bentheimer sandstone becomes a weaker insulator (Table 2).

#### 4. Conclusions

We have investigate the firing of the Bentheimer samples, a commonly used procedure in core preparation, to make the internal rock properties uniform and improve reproducibility of displacement experiments. The petrophysical, petrological pyrometamorphical and electrical properties of unfired and fired samples were measured using various complementary methods. The following main conclusions can be drawn:

In unfired samples, ion exchange between minerals (mainly clays) and injected fluids caused clay migration (kaoline and illite) and swelling (illite and smectite) leading to partial or total plugging. The local clay concentrations, differences in the crystal structure and the interaction of the various constituents were validated by dispersion in the dielectric permittivity over frequencies.

Firing of Bentheimer sandstone above 900 °C led to gradual changes in the samples mineral composition, color, surface roughness and physical properties, through transformation, disintegration and pyrometamorphism of the components.

Fine loose particles were created by thermal disintegration and still may migrate during liquid flow experiments. The conducted XRD study and the decrease in the permittivity value with its insignificant dispersion (~5%) between the high and the low frequencies indicated the clay transformations.

Thermal stresses also caused variation in the pore geometry, change in grain boundaries and contacts and particle cracking, i.e. as a result, the porosity and permeability increased by up to 5% and samples became more friable.

The mechanical strength of cementing material decreased due to dehydration-rehydration and heterogeneous thermal expansion. The boundary between the detrital quartz grains became detached by better connected, larger and wider throats.

Firing resulted in decomposition of minerals with Fe content and caused formation of source of amorphous oxides that influence the wettability. The iron oxides do not directly alter the relative permittivity of the solid phase. However, the correlation exists between the larger specific surface and capillary retention capacity of iron oxides, as compared with quartz grains.

The firing of Bentheimer sandstone cores eliminate problems related to clays, but as well, create fines originated from the destroyed cement that may affect the flow, so reproducibility of experiments might not be possible. Moreover, the change in the equilibria for the altered ion exchange is observed, such that local wettability varies.

#### Acknowledgments

The authors want to thank the CATO program, the Dutch national research program on Carbon Dioxide Capture and Storage, for financial support of the study. The authors are grateful to Dr. Koenraad Elewaut for his valuable comments and help on how to improve the quality of the paper. Furthermore, we appreciate the technical support of the Geoscience and Engineering Laboratory, Jolanda van Haagen, the micro laboratory for the SEM measurements and the High Voltage Laboratory for the use of the dielectric equipment.

#### Appendix A. Supplementary data

Supplementary data associated with this article can be found in the online version at <http://dx.doi.org/10.1016/j.petrol.2016.10.024>.

## References

- Al-Mjeni, R., Günzel, F., Jing, X., Grattoni, C.A., Zimmerman, R.W., The influence of clay fraction on the complex impedance of shaly sands. *Symbolic Computational Algebra* 29.
- Argall, F., Jonscher, A.K., 1968. Dielectric properties of thin films of aluminium oxide and silicon oxide. *Thin Solid Films* 2 (3), 185–210.
- Arora, R., Mosch, W., 2011. *High Voltage and Electrical Insulation Engineering* 69. John Wiley & Sons.
- Arulanandan, K., 2003. *Soil Structure: In Situ Properties and Behavior*, Department of Civil and Environmental Engineering, University of California, Davis, California.
- Barclay, S.A., Worden, R.H., 2009. *Effects of Reservoir Wettability on Quartz Cementation in Oil Fields*, Blackwell Publishing Ltd., 103–117. <http://dx.doi.org/10.1002/9781444304237.ch8>.
- Bartnikas, R., 1987. *Engineering dielectrics: Electrical properties of solid insulating materials: measurement techniques*. Vol. 926, American Society for Testing and Materials, Baltimore.
- Bhargava, S.K., Garg, A., Subasinghe, N.D., 2009. In situ high-temperature phase transformation studies on pyrite. *Fuel* 88 (6), 988–993. <http://dx.doi.org/10.1016/j.fuel.2008.12.005>.
- Brunauer, S., Emmett, P.H., Teller, E., 1938. Adsorption of gases in multimolecular layers. *J. Am. Chem. Soc.* 60 (2), 309–319.
- Carroll, D., *Clay minerals: a guide to their X-ray identification*. Vol. 126, Geological Society of America, Boulder, Colorado, 1970.
- Civan, F., Knapp, R.M., 1987. Effect of clay swelling and fines migration on formation permeability. *Soc. Pet. Eng.* <http://dx.doi.org/10.2118/16235-MS>.
- Curie, J., 1888. Recherches sur le pouvoir inducteur spécifique et sur la conductibilité des corps cristallisés. par M. Jacques Curie, La Lumière électrique.
- Dakin, T.W., 2006. Conduction and polarization mechanisms and trends in dielectric. *IEEE Electr. Insul. Mag.* 22 (5), 11–28. <http://dx.doi.org/10.1109/mei.2006.1705854>.
- De Boever, W., Bultreys T., Traska, M., Mock, A., Brabant, L., Cnudde, V., June 2013. 3D Characterization of the Bentheimer sandstone and Euville Limestone. in relation to fluid flow through their pore networks, 2013, paper presented at the 14th Euro Seminar on Microscopy Applied to Building Materials, Helsingør, Denmark, pp. 10–14
- Friolo, K.H., Ray, A.S., Stuart, B.H., Thomas, P.S., 2005. Thermal analysis of heritage stones. *J. Therm. Anal. Calorim.* 80 (3), 559–563. <http://dx.doi.org/10.1007/s10973-005-0694-6>.
- Gabbott, P., 2008. *Principles and Applications of Thermal Analysis*. John Wiley & Sons.
- Gabriel, G.A., Inamdar, G.R., 1983. An experimental investigation of fines migration in porous media. *Soc. Pet. Eng.* <http://dx.doi.org/10.2118/12168-MS>.
- Garton, C.G., 1941. Dielectric loss in thin films of insulating liquids. *J. Inst. Electr. Eng. Part II Power Eng.* 88 (2), 103–120. <http://dx.doi.org/10.1049/ji-3-1.1941.0006>.
- Ghiorso, M.S., Carmichael, I.S.E., Moret, L.K., 1979. Inverted high-temperature quartz. *Contrib. Mineral. Petrol.* 68 (3), 307–323.
- González, G., Moreira, M.B.C., 1991. The wettability of mineral surfaces containing adsorbed asphaltene. *Colloids Surf.* 58 (3), 293–302. [http://dx.doi.org/10.1016/0166-6622\(91\)80229-H](http://dx.doi.org/10.1016/0166-6622(91)80229-H).
- Gray, D.H., Rex, R.W., 1966. Formation damage in sandstones caused by clay dispersion and migration. *Clays Clay Miner.* 14, 355–366.
- Grim, R.E., 1968. *Clay mineralogy*. McGraw-Hill Book Company, New York.
- Haines, P.J., 2002. *Principles of thermal analysis and calorimetry*. R. Soc. Chem..
- Howell, B., Licastro, P., 1961. Dielectric behavior of rocks and minerals. *Am. Mineral.* 46 (3–4), 269–288.
- Huntley, D., 1986. Relations between permeability and electrical resistivity in granular aquifers. *Ground Water* 24 (4), 466–474. <http://dx.doi.org/10.1111/j.1745-6584.1986.tb01025.x>.
- Ishai, P.B., Talary, M.S., Caduff, A., Levy, E., Feldman, Y., 2013. Electrode polarization in dielectric measurements: a review. *Meas. Sci. Technol.* 24 (10), 102001.
- Ismailov, A.K., 1981. Thermodynamic analysis of the formation of mullite from kaolinite. *Glass Ceram.* 38 (7), 363–364. <http://dx.doi.org/10.1007/bf00710091>.
- Izgorodina, E.I., Forsyth, M., MacFarlane, D.R., 2009. On the components of the dielectric constants of ionic liquids: ionic polarization. *Phys. Chem.* 11 (14), 2452–2458.
- Janusz, W., 1999. *Electrical Double Layer at the Metal Oxide-electrolyte Interface* 85. CRC Press, Taipei, Taiwan.
- Jones, F.O.J., Influence of chemical composition of water on clay blocking of permeability. *Journal of Petroleum Technology* <http://dx.doi.org/10.2118/631-pa>.
- Jonscher, A.K., 1984. *Dielectric Polarisation/depolarisation in Solids*. Dielectric Press, London.
- Kühnel, R.A., 1998. Atlas of minerals and related phases in unaltered and thermally altered materials from the Rocky Mountain 1 underground coal gasification field site: Topical report, Report, Gas Research Institute, North Dakota.
- Klein, E., Reuschlé, T., 2003. A Model for the mechanical behaviour of Bentheim sandstone in the brittle regime. *Pageoph Topical Volumes*, Birkhäuser Basel, Basel, book section 3, pp. 833–849. doi:10.1007/978-3-0348-8083-1\_3.
- Klimentos, T., McCann, C., 1990. Relationships among compressional wave attenuation, porosity, clay content, and permeability in sandstones. *Geo Phys.* 55 (8), 998–1014.
- Krinsley, D.H., Pye, K., Boggs, S., Jr, Tovey, N.K., 2005. *Backscattered Scanning Electron Microscopy and Image Analysis of Sediments and Sedimentary Rocks*. Cambridge University Press.
- Laj, C., Channell, J., 2007. Geomagnetic excursions. *Treatise Geophys.* 5 (373), e416.
- Leroy, P., Revil, A., 2004. A triple-layer model of the surface electrochemical properties of clay minerals. *J. Colloid Interface Sci.* 270 (2), 371–380. <http://dx.doi.org/10.1016/j.jcis.2003.08.007>.
- Lichtenecker, K., Rother, K., 1931. Die Herleitung des logarithmischen Mischungsgesetzes aus allgemeinen Prinzipien der stationären Strömung. *Phys. Z.* 32, 255–260.
- Loahardjo, N., Winoto, W., Morrow, N.R., August 2012. Oil recovery from Bentheim sandstone by sequential waterflooding and spontaneous imbibition Paper presented at the International Society of Core Analysts Annual Meeting, Scotland, pp. 12–22.
- Ma, S., Morrow, N.R., Effect of firing on petrophysical properties of Berea Sandstone. *SPE Formation Evaluation* <http://dx.doi.org/10.2118/21045-pa>.
- Maloney, D.R., Brinkmeyer, A.D., Honarpour, M.M., 1990. Relative permeabilities and other characteristics of 700-millidarcy, fired Berea sandstone, Report, National Institute for Petroleum and Energy Research.
- Mohan, K.K., Fogler, H.S., 1997. Effect of pH and layer charge on formation damage in porous media containing swelling clays. *Langmuir* 13 (10), 2863–2872. <http://dx.doi.org/10.1021/la960868w>.
- Mohan, K.K., Vaitya, R.N., Reed, M.G., Fogler, H.S., 1993. Water sensitivity of sandstones containing swelling and non-swelling clays. *Colloids Surf. A Physicochem. Eng. Asp.* 73, 237–254.
- Moore, D.M., Reynolds, R.C., 1989. *X-ray Diffraction and the Identification and Analysis of Clay Minerals* 378. Oxford University Press, Oxford.
- Morse, J.G., 2013. *Nuclear Methods in Mineral Exploration and Production* 7. Elsevier.
- Nabighian, M.N., 1987. *Electromagnetic methods in applied geophysics: theory*. Vol. 1, Society of Exploration Geophysicists, Tulsa, Oklahoma.
- Neasham, J.W., 1977. The morphology of dispersed clay in sandstone reservoirs and its effect on sandstone shaliness, pore space and fluid flow properties. *Soc. Pet. Eng.* <http://dx.doi.org/10.2118/6858-MS>.
- Norrish, K., 1954. The swelling of montmorillonite. *Discuss. Faraday Soc.* 18 (0), 120–134. <http://dx.doi.org/10.1039/df9541800120>.
- Olafuyi, O.A., Sheppard, A.P., Arns, C.H., Sok, R.M., Cinar, Y., Knackstedt, M.A., Pinczewski, V.V., 2010. Experimental verification of effect of size on drainage capillary pressure computed from digitized tomographic images. *Int. J. Eng. Res. Afr.* 1, 1–10.
- Peksa, A.E., Wolf, K.-H.A.A., Zitha, P.L.J., 2015. Bentheimer sandstone revisited for experimental purposes. *Mar. Pet. Geol.* 67 (0), 701–719. <http://dx.doi.org/10.1016/j.marpetgeo.2015.06.001>.
- Potts, D.E., Kuehne, D.L., 1988. Strategy for alkaline/polymer flood design with Berea and reservoir-rock corefloods. *SPE Reserv. Eng.* 3 (04), 1143–1152.
- Prasad, S.V.S., Sitakara Rao, V., 1984. Thermal transformation of iron (III) oxide hydrate gel. *J. Mater. Sci.* 19 (10), 3266–3270. <http://dx.doi.org/10.1007/bf00549813>.
- Rao, K.V., Smakula, A., 1965. Dielectric properties of cobalt oxide, nickel oxide, and their mixed crystals. *J. Appl. Phys.* 36 (6), 2031–2038. <http://dx.doi.org/10.1063/1.1714397>.
- Ruedrich, J., Siegesmund, S., 2007. Salt and ice crystallisation in porous sandstones. *Environ. Geol.* 52 (2), 225–249. <http://dx.doi.org/10.1007/s00254-006-0585-6>.
- Saint-Amant, M., Strangway, D.W., 1970. Dielectric properties of dry, geologic materials. *Geophysics* 35 (4), 624–645.
- Schramm, L.L., Mannhardt, K., Novosad, J.J., 1991. Electrokinetic properties of reservoir rock particles. *Colloids Surf.* 55 (0), 309–331. [http://dx.doi.org/10.1016/0166-6622\(91\)80102-T](http://dx.doi.org/10.1016/0166-6622(91)80102-T).
- Schweidler, E.R.V., 1907. Studien über die Anomalien im Verhalten der Dielektrika. *Ann. Phys.* 329, 711–770.
- Selley, R.C., Sonnenberg, S.A., 2014. *Elements of Petroleum Geology*. Academic Press.
- Sengwa, R.J., Soni, A., 2006. Low-frequency dielectric dispersion and microwave dielectric properties of dry and water-saturated limestones of Jodhpur region. *Geophysics* 71 (5), G269–G277.
- Sharma, M.M., Yortsos, Y.C., 1987. Fines migration in porous media. *J. Am. Chem. Soc.* 33 (10), 1654–1662. <http://dx.doi.org/10.1002/aic.690331009>.
- Sharma, C.L., Nath, M., Bharti, N., 1994. Thermal studies on praseodymium-iron (1:9 wt %) oxyhydroxide. *J. Mater. Sci. Lett.* 13 (14), 1010–1011. <http://dx.doi.org/10.1007/bf00277023>.
- Shaw, J.C., Churcher, P.L., Hawkins, B.F., The effect of firing on Berea Sandstone, *SPE Formation Evaluation* <http://dx.doi.org/10.2118/18463-pa>.
- Somerton, W.H., 1992. *Thermal Properties and Temperature-related Behavior of Rock/fluid Systems* 37. Elsevier Science, New York.
- Sumner, M.E., 1963. Effect of iron oxides on positive and negative charges in clays and soils. *Clay Min. Bull.* 5 (29), 218–226.
- Sydansk, R.D., Discussion of the effect of temperature and confining pressure on single-phase flow in consolidated rocks. *Journal of Petroleum Technology and Alternative Fuels* 32 (8).
- Tiab, D., Donaldson, E.C., 2015. *Petrophysics: Theory and Practice of Measuring Reservoir Rock and Fluid Transport Properties*. Gulf professional publishing.
- Van Dam, R.L., Schlager, W., Dekkers, M.J., Huisman, J.A., 2002. Iron oxides as a cause of GPR reflections. *Geophysics* 67 (2), 536–545.
- Wang, F.H.L., Guidry, L.J., 1994. Effect of oxidation-reduction condition on wettability alteration. *SPE Form. Eval.* 9 (02), 140–148.
- Wildenschild, D., Roberts, J.J., Carlberg, E.D., 1999. Electrical properties of sand-clay mixtures: the effect of microstructure Paper presented at the International Exposition and 69th Annual Meeting of the Society of Exploration Geophysicists. Houston, Texas, 31 October–5 November.
- Wolf, K.H., 2006. The interaction between underground coal fires and their roof rocks, Dissertation. Delft University of Technology, Delft, The Netherlands.
- Wu, S., Firoozabadi, A., 2010. Effects of firing and chemical treatments on Berea permeability and wettability. *Energy Fuels* 25 (1), 197–207. <http://dx.doi.org/10.1021/ef1007984>.